

# MEASURING GALAXY CLUSTERING WITH FAR-IR LINE INTENSITY MAPPING

B. D. UZGIL<sup>1,2</sup>, J. E. AGUIRRE<sup>1</sup>, AND C. M. BRADFORD<sup>2</sup>

*Draft version March 10, 2014*

## ABSTRACT

a new technique to measure galaxy clustering without individual detections of galaxies. We develop robust predictions of line specific intensity for a suite of astrophysically interesting lines and make predictions about the detectability of the clustering signal via the 3D power spectrum of a data cube, where the galaxies need not be either spatially or spectrally resolved. We show that line intensity mapping is an efficient method for imaging spectrometers like SPICA/SAFARI to obtain galaxy clustering measurements down to  $k < 0.1 \text{ hMpc}^{-1}$  and out as far as  $z \sim 3$ .

*Subject headings:* far-infrared spectroscopy; galaxy redshift surveys

## 1. INTRODUCTION

Intensity mapping is a *statistical* analysis of the spatial fluctuations in spectral line emission, whereby a survey of spectral lines at different frequencies produces a fully three dimensional data cube containing “tomographic scans” of the Universe along the spectral (i.e., redshift) direction and is decomposed into its power spectrum. Atomic (Gong et al 2012, Visbal et al 2011, etc.) and molecular (Lidz et al 2011, Gong et al 2012 etc.) transitions – such as the 21 cm spin flip transition from H<sup>o</sup>, CO (2-1), and [CII] 158 $\mu\text{m}$  – have been investigated as candidates for intensity mapping experiments during the Epoch of Reionization. Of these, the neutral hydrogen case is undoubtedly the most developed in terms of its standing in the literature (cf. Furlanetto, Oh, and Briggs for a review) and in the experimental arena (e.g., PAPER (Parsons et al 2010), MWA), and so interest in measuring the [CII] power spectrum, for instance, primarily erupted as a means to complement the 21 cm studies at high redshift via the cross-correlation.

As a proof of principal, the appeal of intensity mapping experiments in the post-Reionization era is obvious. Neutral hydrogen is, again, the most mature in this respect, as 21cm experiments have successfully measured the 21cm-galaxy cross power spectrum (Chang et al 201) or put limits on the 21cm auto-power (Switzer et al 2013), but the detectability of another transition Hydrogen transition, the Ly $\alpha$  line, has also been explored in Pullen et al for redshifts from before Reionization down to  $z \sim 2$ .

Here we examine the application of the intensity mapping technique to moderate redshifts, targeting the fine structure line emission from ionized carbon in the interstellar medium of star-forming galaxies during  $0.5 < z < 1.5$ . The [CII]158 $\mu\text{m}$  line is a well-suited probe of the galaxy population during this time frame, as the mean dust attenuation in galaxies peaks at  $z \sim 1.5$ , when roughly 80% of the cosmic star formation rate density is obscured and captured only in the infrared emission of re-processed starlight by dust grains (Burgarella et al 2013). Moreover, this line is typically the brightest FIR emitted from the ISM of galaxies, with luminosities up

0.1% of the IR luminosity, and is an important sign-post of star formation and related dynamics in galaxies (DeLooze et al, Diaz-Santos, et al).

Due to the spatio-spectral nature of intensity mapping, this technique as applied to [CII] line intensity fluctuations can be a highly complementary probe to recent studies of the 2-dimensional clustering properties of dusty, star-forming galaxies (DSFGs) (see Casey et al 2014 for a review). These studies, using a modification of the “ $P(D)$ ” approach, for example by (??), have already shed light on some aspects of the clustering of the most extreme star-forming system from  $z = 1 - 3$ , but they are limited by the lack of redshift information, and by the need to include “nuisance parameters” in their estimation of the halo model. From the far-IR to the millimeter, it remains for the future for ALMA or NOEMA to produce redshift surveys with  $\sim 10^3$  galaxies, or even further down the road for CCAT. Thus we present a novel method of characterizing the 3D clustering of DSFGs with [CII] intensity mapping, which, importantly, does not rely on detecting individual galaxies in order to measure the power spectrum with high significance.

Furthermore, this sensitivity of the power spectrum to galaxies which are below the threshold for individual detections by current and future instruments—paired with the fact that the amplitude of the power spectrum is proportional on large scales to the mean intensity of the target line—introduces astrophysically interesting information inherent in the intensity mapping technique, in addition to the previously discussed statistical characterization of galaxy clustering. Namely, by extracting the mean intensity of [CII], or any emission line of interest, from the power spectrum at a number of observed frequencies, intensity mapping provides a means of quantifying the evolution of aggregate line emission over cosmic time.

The organization of this paper is as follows. We have calculated the mean intensity for a suite of fine structure IR emission lines, including the [CII] line, based on the IR luminosity function and empirical line-to-IR luminosity correlations, and present these results in the context of a power spectrum model in Section 2. In Section 3, we envision a suitable platform—namely, a balloon-borne experiment operating at frequencies between 240 $\mu\text{m}$  to 420 $\mu\text{m}$ —for conducting the [CII] inten-

badeu@sas.upenn.edu

<sup>1</sup> University of Pennsylvania, Philadelphia, PA 19104

<sup>2</sup> Jet Propulsion Laboratory

sity mapping experiment and discuss the feasibility of detecting the [CII] power spectra in terms of the Signal-to-Noise Ratio. From the power spectra, we provide estimates for accuracy on measuring the mean [CII] intensity as a function of redshift. To better assess the value of intensity mapping studies in the case of [CII] at moderate redshifts, and of intensity mapping experiments in general, we compare in Section 4 the performance of the intensity mapping approach against spectroscopic galaxy surveys that rely on individual detections of sources to measure the power spectrum.

## 2. SETTING UP PREDICTIONS FOR FAR-IR LINE POWER SPECTRA DURING $0.5 < Z < 3$

Conventional methods for measuring the spatial autocorrelation of galaxies through galaxy surveys rely on the knowledge of the redshift distribution of sources in the survey. Furthermore, they estimate the true three dimensional clustering of galaxies via the angular projection. Intensity mapping, however, contains intrinsic redshift information and provides a direct measure of the clustering power spectrum in three-dimensional  $k$ -space, which makes it a highly complementary probe of structure in the cosmic web.

The complete auto power spectrum of a given FIR line as a function of wavenumber  $k$ ,  $P_{i,i}(k, z)$ , can be separated into power from the clustering of galaxies,  $P_{i,i}^{clust}(k, z)$  and a Poisson term describing their discrete nature,  $P_{i,i}^{shot}(z)$ . We compute the full nonlinear matter power spectrum,  $P_m(k, z)$ , using the publicly available code HALOFIT+, which has been the standard tool for predicting matter power spectra upon its success in fitting state-of-the-art dark matter simulations over a decade ago (Smith et al 2003). (We note in passing, however, that since that time, authors (cf., e.g., Takahashi et al 2012) have pointed out improvements to the halo model fit on the small scales previously inaccessible due to constraints on simulation resolution.) The clustering component of the line power spectrum is then written as

$$P_{i,i}^{clust}(k, z) = \bar{S}_i^2(z) \bar{b}_i^2(z) P_{\delta\delta}(k, z). \quad (1)$$

Here we have implicitly assumed that the fluctuations in line emission trace the matter power spectrum with some average bias,  $\bar{b}_i(z)$ . The mean line intensity,  $\bar{S}_i(z)$ , in units of  $\text{Jy sr}^{-1}$ , can be calculated as

$$\bar{S}_i(z) = \int dn_i \frac{L_i}{4\pi D_L^2} y_i D_A^2, \quad (2)$$

where the integration is taken with respect to  $n_i$ , the number of galactic line emitters per cosmological comoving volume element. (The factor  $y_i$  is the derivative of the comoving radial distance with respect to the observed frequency, i.e.  $y = d\chi/d\nu = \lambda_{i,rest}(1+z)^2/H(z)$ , and  $D_A$  is the comoving angular distance.)

Finally, the shot noise component of the total line power spectrum—with the same units as the clustering term, namely,  $\text{Jy}^2 \text{sr}^{-2} (\text{Mpc h}^{-1})^3$ —takes the form

$$P_{i,i}^{shot}(z) = \int dn_i \left( \frac{L_i}{4\pi D_L^2} \right)^2 (y_i D_A^2)^2. \quad (3)$$

### 2.1. Calculating IR line volume emissivity

The number density of line emitters and the line luminosity that appear in equations (2) and (3) can be derived by a variety of methods. In earlier papers on intensity mapping of molecular and fine-structure emission lines at high redshift ( $z \gtrsim 6$ ), one approach involved using the dark matter halo mass function in lieu of the line emitter density (and invoking a one-to-one correlation between halos and galaxies, which is not unreasonable at high redshifts). The line luminosity, in turn, could be scaled according to the star formation rate, which was related to halo mass via a proportionality constant comprised of factors that described the fraction of baryons available for star formation, as well as the dynamical timescale for star formation and a duty cycle for emission. While this theoretical model is feasible at high redshift to provide an estimate on the mean intensity  $\bar{S}_i$ , we take advantage of the relative wealth of observations of [CII] luminosities in individual galaxies, IR galaxy number counts, and cosmic star formation rate density at the lower redshifts relevant to this study. To this end, we first employ the empirically-constrained, backwards-evolution model of the IR luminosity function  $\Phi(L_{IR}, z)$  from Bethermin et al (2011, hereafter B11) to predict the number of galaxies with luminosity  $L_{IR}$  at a given redshift in some comoving volume of the Universe per logarithmic luminosity interval, i.e.,  $\frac{dN(L_{IR}, z)}{dV d\log_{10} L_{IR}}$  or  $\frac{dn_{IR}}{d\log_{10} L_{IR}}$ . One major drawback of our empirical approach is that it does not allow us to model the bias in a self-contained manner, e.g., such as in the halo model formalism that other predictions, which connect  $L_{IR}$  to halo mass, employ.

To convert the infrared luminosity to a line luminosity, we apply the relation for  $L_i$  as a function of  $L_{IR}$  provided by Spinoglio et al (2012). The fit in their paper was based on the collection of ISO-LWS observations of local galaxies in Brauer et al (2008), and is reproduced below for [CII]:

$$L_{[\text{CII}]158}(L_{IR}) = (0.89 \pm 0.03) \log_{10} L_{IR} - (2.44 \pm 0.07) \quad (4)$$

Thus, it becomes possible to write the cosmic mean intensity and shot noise of the line, in units of  $\text{Jy sr}^{-1}$ , as a function of redshift based on the B11 luminosity function and Spinoglio et al (2012)  $L_i - L_{IR}$  relation as

$$\bar{S}_i(z) = \int_{L_{IR, min}}^{L_{IR, max}} d\log L_{IR} \Phi(L_{IR}, z) \frac{f_i L_{IR}}{4\pi D_L^2} y D_A^2 \quad (5)$$

$$P_{i,i}^{shot}(z) = \int_{L_{IR, min}}^{L_{IR, max}} d\log L_{IR} \Phi(L_{IR}, z) \left( \frac{f_i L_{IR}}{4\pi D_L^2} y D_A^2 \right)^2 \quad (6)$$

where  $f_i$ , i.e.  $\frac{L_i(L_{IR})}{L_{IR}}$ , is the fraction of IR luminosity emitted in line  $i$ , as computed from equation (3). In other words, we have written  $\bar{S}_i$  and  $P_{i,i}^{shot}(z)$  as the first and the second moments of the luminosity function.

It should be noted that the mean line luminosity  $\bar{L}_i$  does, in reality, include a contribution from diffuse gas in the intergalactic medium (IGM), yet Gong et al (2012) estimated that the specific intensity of one of the brightest lines typically observed in galaxies, namely [CII],

coming from the IGM ranges from  $\sim 10^{-3}$  Jy sr $^{-1}$  to  $\sim 1$  Jy sr $^{-1}$  for different physical conditions in the ISM at  $z = 1$ —a negligible amount compared to the emission from the interstellar medium (ISM) of galaxies.

The resulting mean intensities for a variety of FIR lines are plotted in Figure 1 as functions of redshift and observed frequency.  $\bar{S}_\nu$  vs  $\lambda_{obs}$  can be interpreted as identifying the dominant source of fluctuations, according to our model, for a given frequency. As a specific example, if the target line of an observation is [OI]63 $\mu$ m at  $z = 1$ , it is necessary to distinguish between the target line and interlopers from different redshifts which nonetheless contribute power at the observed frequency. Visbal and Loeb (2010) showed how the cross spectra can be used to differentiate between a target line and a contaminating line (or “bad line”, in their words), since emitters at different redshifts will be spatially uncorrelated. For the observed wavelengths of [CII], however, it is apparent from Figure 2 that, with the exception of contributions from [OIII]88 $\mu$ m near  $z \sim 0.01$ , the [CII] line is not vulnerable to confusion with interlopers.

### 3. THE [CII] POWER SPECTRUM

#### 3.1. Sensitivity forecast

We present in this section predictions for the [CII] power spectrum with error bar estimates for a feasible experimental platform, namely, a balloon-borne experiment with uninterrupted spectral coverage in the wavelength range 240 to 420  $\mu$ m. Fiducial experimental parameters are summarized in Table 1. The telescope mirror aperture,  $D_{ap}$ , survey area,  $A_{survey}$ , and total observing time,  $t_{obs}^{survey}$ , are taken as 2.5 m, 1 deg $^2$ , and 200 hours, respectively, though we explore the effect of varying  $D_{ap}$  and  $A_{survey}$  on SNR (cf. Figure 3).

Predictions for the fiducial case—as computed from the method of combining the cosmological matter power spectrum and the IR LF model outlined in Section 2.1—for the [CII] power spectrum at four redshifts  $z = 0.63, 0.88, 1.16$ , and  $1.48$  are shown in Figure 2. (Note that we use  $\Delta_{[CII],[CII]}^2 = k^3 P_{[CII],[CII]}(k) / (2\pi^2)$  when plotting the power spectrum. In this notation, the factor  $k^3$  cancels out the volumetric units of  $P_{\delta,\delta}(k, z)$  and the integral of  $\Delta_{[CII],[CII]}^2$  over logarithmic  $k$  bins is equal to the variance in real space.) At these redshifts, respectively, the average linear bias has been assumed to be  $\bar{b} = 2.0, 2.3, 2.6$ , and  $2.9$ , in line with theoretical predictions from (Cooray and Sheth ???). The crossing of the one-halo and two-halo terms in the power spectrum can be detected with SNR of order 10 at all redshifts. In calculating the power spectrum sensitivity, the two lowest line-of-sight modes and the lowest transverse mode are not included, since these modes will likely be compromised by the necessity of continuum foreground subtraction and beam-differencing in the fluctuation analysis. The exact effect of continuum subtraction will need to be modeled via simulation.

Error bar estimates and the total SNR for the power spectrum are calculated by assuming a spectrally flat noise power spectrum, so that the noise power in each pixel,  $P_N$ , is written as

$$P_N = \sigma_N^2 \frac{V_{pix}}{t_{pix}}, \quad (7)$$

where  $\sigma_N^2$  is the instrument sensitivity (noise equivalent intensity, or NEI, in units of Jy sr $^{-1}$  s $^{1/2}$ ),  $V_{pix}$  is the volume of a pixel, and  $t_{obs}^{pix}$  is the time spent observing on a single pixel. The variance of a measured  $k$ ,  $\sigma^2(k)$ , is then written as

$$\sigma^2(k) = \frac{(P_{[CII],[CII]}(k) + P_N(k))^2}{N_{modes}}, \quad (8)$$

where  $N_{modes}$  is the number of wavemodes that are sampled for a given  $k$  bin of some finite width  $\Delta \log(k)$ . (We have chosen  $\Delta \log(k) = 0.3$  for this analysis.)

The total SNR, in turn, is calculated from the expression

$$SNR_{tot} = \sqrt{\sum_{bins} \left( \frac{P_{[CII],[CII]}(k)}{\sigma(k)} \right)^2} \quad (9)$$

Note that it is possible to rewrite  $P_N$  in terms of the parameters from Table 1, giving

$$\begin{aligned} P_N &= \left( \sigma_N^2 A_{pix} \Delta r_{los}^{pix} \right) / \left( \frac{t_{survey}}{n_{beams} / N_{instr}^{spatial}} \right) \\ &= \left( \sigma_N^2 A_{pix} \Delta r_{los}^{pix} \right) / \left( \frac{t_{survey} N_{instr}^{spatial}}{A_{survey} / A_{pix}} \right) \\ &= \sigma_N^2 \frac{\Delta r_{los}^{pix} A_{survey}}{t_{survey} N_{instr}^{spatial}} \end{aligned} \quad (10)$$

In this form, it becomes apparent that—with fixed number of spatial pixels, spectral resolution, and total observing time—the only factor driving up the amplitude of noise power is the survey area; the effect of increasing aperture only allows access to higher wavenumbers, which can be useful for subtracting the shot noise from the total power in later steps of data analysis. This behavior is shown clearly in Figure 5, where the SNR is plotted as a function of  $k$  for different survey geometries and both mirror diameters. Also seen in Figure 5, the greater number of wavemodes sampled (entering as  $N_{modes}^{-1/2}$  in the expression for  $\sigma$ ) with the larger survey area does not necessarily compensate for the increase in  $P_N$ . For example, the factor of ten increase in  $P_N$  going from  $A_{survey} = 1$  to  $10$  deg $^2$  is only overcome by the additional modes in the larger survey area for  $k < 1$ , leading to a higher S/N for these modes. At  $k > 1$ , the S/N in each mode for the 1 and 10 deg $^2$  fields becomes comparable.

#### 3.2. Measuring $\bar{S}_{[CII]}(z)$

Recall that the [CII] clustering power spectrum  $P_{[CII],[CII]}^{clust}$  as measured by intensity mapping is sensitive to intensity fluctuations from the full range of normal to ULIRG-class systems because its amplitude is proportional to the mean line intensity,  $\bar{S}_{[CII]}$ :  $P_{[CII],[CII]}^{clust} = \bar{S}_{[CII]}^2 \bar{b}^2 P_{\delta,\delta}$ . In order to successfully extract  $\bar{S}_{[CII]}$  from the power spectrum, then, it is necessary to divide out  $P_{\delta,\delta}(k, z)$  and  $\bar{b}_{[CII]}(z)$ . (High sensitivity on shot noise-

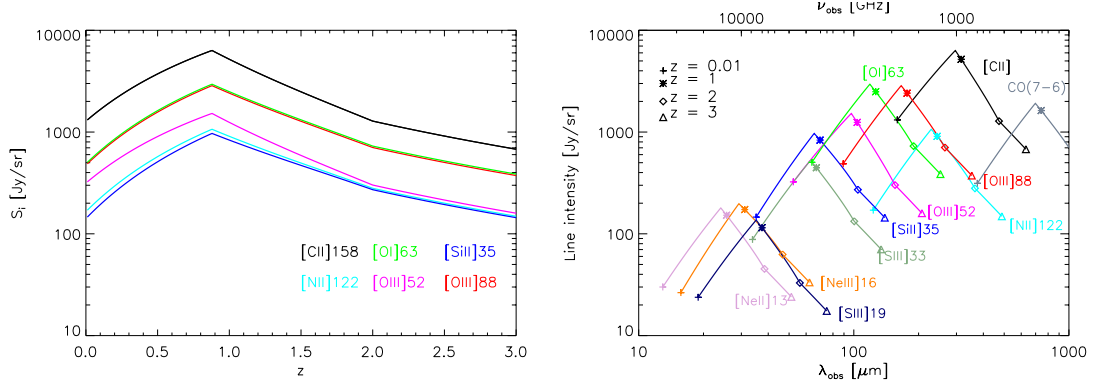


FIG. 1.—: Intensity of fine structure line emission plotted versus redshift (*top*) and observed wavelength (*bottom*) as predicted from Spinoglio line luminosity fits as applied to the B11 luminosity function.

TABLE 1: Fiducial Parameters for Envisioned Balloon Experiment

$R = \nu_{obs}/\delta\nu$	450			
$t_{survey}^{obs}$ (hr)	200			
$D_{ap}$ (m)	2.5			
$A_{survey}$ (deg <sup>2</sup> )	1.0			
$z$	0.63	0.88	1.16	1.48
$\bar{S}_{[CII]}$ (Jy sr <sup>-1</sup> )	$4.56 \times 10^3$	$6.33 \times 10^3$	$4.05 \times 10^3$	$2.55 \times 10^3$
NEI ( $10^7$ Jy sr <sup>-1</sup> sec <sup>1/2</sup> )	3.4	2.1	1.5	1.0
Line Sensitivity ( $10^{-17}$ W m <sup>-2</sup> sec <sup>1/2</sup> )	1.58	1.13	0.92	0.71
Wavelength Range ( $\mu$ m)	240-276	276-317	317-365	365 - 420
$\delta\nu$ (GHz)	2.58	2.25	1.95	1.70

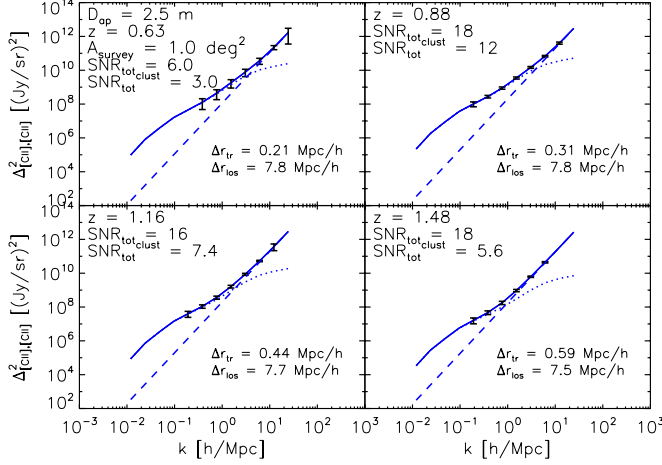


FIG. 2.—: Predicted [CII] power spectra with error bar estimates from  $z = 0.63$  to  $z = 1.48$  for telescope with 2.5 meter aperture and a survey area of 1 square degree. Dotted curves indicate power from clustering (including contributions from linear and nonlinear terms), and dashed curves indicate the contribution from shot noise power.

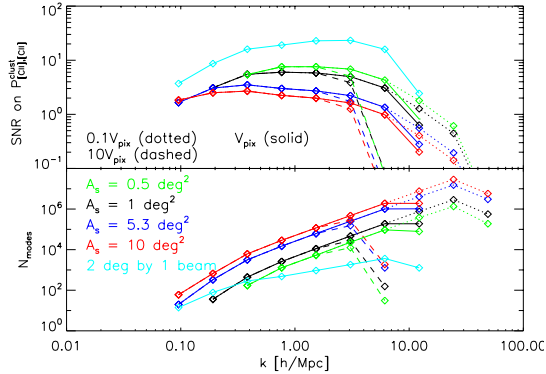


FIG. 3.—: Signal to noise on the clustering term of the [CII] power spectrum  $P_{[CII], [CII]}$  and number of modes as a function of  $k$  at  $z = 0.88$ . The black, blue, and red lines correspond to survey areas of 1.0, 5.3, and 10.0  $\text{deg}^2$ , respectively. Telescopes with apertures yielding 0.1, 1, and 10 times the fiducial pixel volume,  $V_{pix}$ , are shown as the dotted, solid, and dashed lines, respectively.

dominated modes ensures that the preliminary step of accurate shot noise subtraction is readily attainable.) The confidence with which these are *a priori* known quantities becomes lower as  $k$  increases. For example, the 1-halo power spectrum for DSFGs appears to be dependent on  $L_{IR}$  of the contributing sources (Viero et al 2013), indicating the need to map sufficiently wide areas that access  $k$  modes dominated by the linear 2-halo term.

Returning to Figure 3, we see that, for the purpose of measuring  $\bar{S}_{[CII]}$ ,  $A_{survey}$  must be greater than our fiducial value of 1  $\text{deg}^2$  so that there are at least three  $k$  bins, namely,  $k = 0.08, 0.16$ , and  $0.32$  h/Mpc, with the power from halo-halo clustering accounting for 75% or greater of the total power at each  $k$ , for each observed redshift<sup>3</sup>.

<sup>3</sup> The only exception is for  $z = 0.63$ , for which the 5.3  $\text{deg}^2$

Thus, in considering the case of  $A_{survey} = 5.3 \text{ deg}^2$ , we find that it is possible to measure  $\bar{S}_{[CII]}(z)$  within  $\sim 10\%$  accuracy from  $z = 0.63$  to  $z = 1.5$ , as shown in Figure 4, where the fractional uncertainty on  $\bar{S}_{[CII]}(z)$  has been calculated as half the fractional uncertainty on  $P_{[CII], [CII]}(k, z)$ . For this scenario, we have adopted an observing time achievable in ultra long duration balloon flights, namely,  $t_{obs}^{survey} = 1,000$  hr, which increases the sensitivities reported in the fiducial case by a factor of 5.

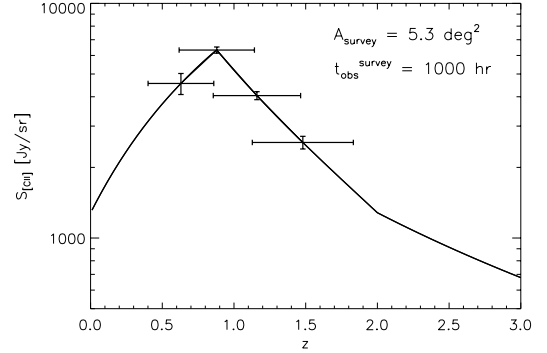


FIG. 4.—: Error bar estimates on  $\bar{S}_{[CII]}$ , as measured by the fiducial instrument for  $A_{survey} = 5.3 \text{ deg}^2$  and  $t_{obs}^{survey} = 1,000$  hr, at observed redshifts  $z = 0.63, 0.88, 1.16$ , and  $1.48$ . Errors in  $z$  correspond to the redshift space spanned by the spectrometer bandwidth. The solid curve is the underlying model for [CII] mean intensity.

#### 4. OBSERVATIONAL STRATEGY

Now let us turn to a question regarding the motivation for intensity mapping in general, as well as in the specific case of [CII] at the redshifts relevant to this study. Having identified the galaxy redshift surveys as an alternative method to measure the 3D clustering power spectrum, it is natural to ask: In which regime does intensity mapping measure the power spectrum with higher SNR than the traditional galaxy surveys?

The expressions for SNR on a  $k$  bin of interest for galaxy and intensity mapping surveys (denoted, respectively, by the subscripts “GS” and “IM”) are

$$\text{SNR}_{GS} = \frac{\sqrt{N_{modes}}}{1 + 1/(b_i^2 P_{\delta, \delta} \bar{n}_{gal})} \quad (11)$$

$$\text{SNR}_{IM} = \frac{\sqrt{N_{modes}}}{1 + P_N / (\bar{S}_i^2 b_i^2 P_{\delta, \delta})} \quad (12)$$

To facilitate our comparisons in what follows, we employ toy models for the IR LF (Figure 5) written in the Schechter formalism—parametrized by the usual  $\alpha$ ,  $L_*$ , and  $\phi_*$ —and normalize the total luminosity density to the empirical model from Section 2 (cf. Appendix for details). We stress that these Schechter models are not intended to represent a real interpretation of the distribution of galaxies, but are merely helpful for illustrating the effect of the LF *shape* on the relative usefulness of intensity mapping and traditional galaxy surveys.

survey observes modes down to  $k = 0.08$  and  $0.16$  h/Mpc only.

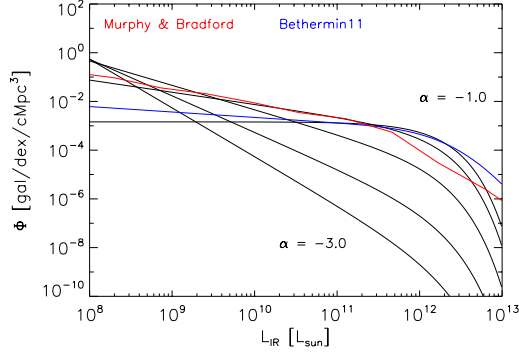


FIG. 5.—: Toy model IR luminosity functions with faint-end slope (from top to bottom)  $\alpha = -1.0, -1.5, -2.0, -2.5, -3.0$ . The B11 and Murphy & Bradford models are plotted as blue and red curves, respectively, for comparison.

The line sensitivity,  $S_\gamma$  (units of  $\text{W m}^{-2} \text{s}^{1/2}$ ), is the figure of merit for detecting an unresolved line in a point source, and we define individual detections at the  $5\sigma$  level as having a flux above the instrumental noise in a pixel, i.e., above  $5 \times S_\gamma t_{\text{pix}}^{-1/2}$ . (For this analysis, we have assumed the galaxy surveys have reliable spectroscopic redshifts and thus neglect the problem of confusion noise.)

Since the intensity mapping technique contains information in the power spectrum from sources below a given  $S_\gamma$ , we expect that regimes in which the majority of galaxies are too faint to be resolved are better-suited for intensity mapping observations than observations via the traditional galaxy survey.

One such regime is when the bulk of the galaxy number density at a certain redshift is comprised of galaxies with sub- $L_*$  luminosities (i.e., for steep slope  $\alpha$  in the LF). Indeed, this case is illustrated in the middle and righthand panels of Figure 7, where, for LFs with  $\alpha < -1.5$ , the intensity mapping method (magenta curve) has higher SNR than the corresponding galaxy survey performed with the same instrument (dashed black curve), for all survey observing times. (Note the galaxy survey and intensity mapping survey map the same fiducial area in this example.) However, for the flattest faint-end slope ( $\alpha = -1$ , lefthand panel), both techniques have comparable SNR for most observing times. We point out that  $\text{SNR}_{\text{IM}} > \text{SNR}_{\text{GS}}$  for very short and very long observing times, which correspond to shot-noise dominated and cosmic variance-dominated regimes, respectively, for the galaxy surveys.

Figure 7 also shows the effect of changing pixel area by a factor  $\epsilon$ —due to a change in the telescope’s aperture diameter by  $\epsilon^{-1/2}$ —on the SNR. Because the area of the survey is fixed, the transformation on pixel area leads to a change in  $S_\gamma$  by the same factor  $\epsilon$ , *but will not alter*  $P_N$  (as seen previously in Eq. 10) for the intensity mapping experiment;  $\text{SNR}_{\text{IM}}$  is robust to changes in pixel area. Thus, the instruments with smaller pixels (triple-dot

dashed curve,  $\epsilon = 0.1$ ) achieve greater depths than their large pixel counterparts (dot-dashed curve,  $\epsilon = 10.0$ ), and thus attain higher SNR by resolving more galaxies. Meanwhile, galaxy surveys with large pixels find themselves in the disabling condition of having many sources

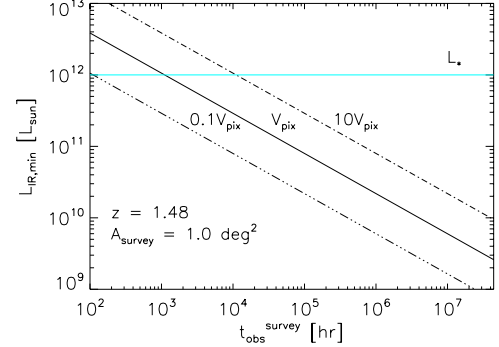


FIG. 6.—:  $L_{\text{IR},\text{min}}$  as a function of the survey observing time, for the various  $V_{\text{pix}}$ , at  $z = 1.5$ . The value of our adopted  $L_*$  is plotted for comparison.

that are below the detection threshold in a single voxel. Whether or not the galaxy survey experiments with small pixel area outperform the intensity mapping experiment is, however, dependent on the faint-end slope of the luminosity function.

In Figure 8,  $\text{SNR}_{\text{GS}}$  is broken down in terms of the number of  $5\sigma$  detections (left panel) and the observed [CII] luminosity density,  $\rho_{[\text{CII}],\text{obs}}$ , relative to the total [CII] luminosity density,  $\rho_{[\text{CII}]}$  (right panel). While it is possible to reach  $\text{SNR}_{\text{GS}} \sim 10$  with  $\sim 100$  galaxies in 200 hours with the fiducial instrument and survey area, the actual fraction of [CII] emission supplied by these detected galaxies is close to 20%. To recover 50% or greater of  $\rho_{[\text{CII}]}$  one must observe for longer than several thousand hours. (For LFs with slopes steeper than  $\alpha = -1.0$ , the required observing times are significantly longer due to the larger population of faint galaxies.) If, however, one extracts the aggregate, unresolved emission from [CII] via the intensity mapped power spectrum, one is essentially measuring  $\frac{\rho_{[\text{CII}],\text{obs}}}{\rho_{[\text{CII}]}} = 1$  as soon as  $\text{SNR}_{\text{IM}}$  on the linear clustering term of the power spectrum is sufficiently high, which we depict in Figure 4 for a  $5.3 \text{ deg}^2$  survey with  $t_{\text{obs}}^{\text{survey}} = 1,000 \text{ hr}$ .

Figure 9 shows the fraction of total [CII] intensity recovered by integrating Eq. 5 with different lower limits on the IR luminosity,  $L_{\text{IR},\text{min}}$ , calculated up to  $z = 3$  for our empirically-based model. (The upper limit,  $L_{\text{IR},\text{max}}$  stays fixed at  $10^{13} L_\odot$ .) If one identifies the  $L_{\text{IR},\text{min}}$  with the detection threshold ( $5\sigma - 1 \text{ hr}$ ) for a particular galaxy survey, then Figure 3 illustrates the depth necessary to achieve in order for a survey to resolve a given fraction of the [CII] emission. Specifically, to resolve at least half of  $\bar{S}_{[\text{CII}]}$ , galaxy surveys must be capable of integrating to depths of  $10^{11}$ ,  $2 \times 10^{11}$ ,  $6 \times 10^{11}$ , and  $10^{12} L_\odot$  for redshifts  $z = 0.6, 1.0, 1.5$ , and  $3$ , respectively.

On the other hand, the

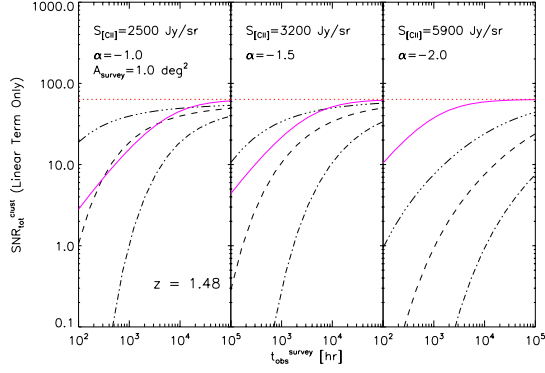


FIG. 7.—: Total Signal-to-Noise ratio ( $\text{SNR}_{tot}$ ) on the linear portion of the clustering power spectrum of [CII] at  $z = 1.5$  as a function of the survey observing time (in hours).  $\text{SNR}_{tot}$  as computed from intensity mapping—which depends only on the integral of the luminosity function, and not the shape—and from the Schechter function models are plotted. Magenta curves represent the intensity mapping experiment. Black Triple-dot-dashed, dashed, and dot-dashed lines correspond to galaxy survey experiments with pixel volumes 0.1, 1.0, 10.0 times the fiducial value. The horizontal dotted red line is the maximum SNR, set by the number of modes in the survey volume. Note that the mean [CII] intensity is increasing for decreasing faint-end slopes, which is a consequence of fixing the total IR light for a given Schechter model to the B11 value, and then applying the  $L_{[CII]} - L_{IR}$  relation to predict [CII] luminosity.

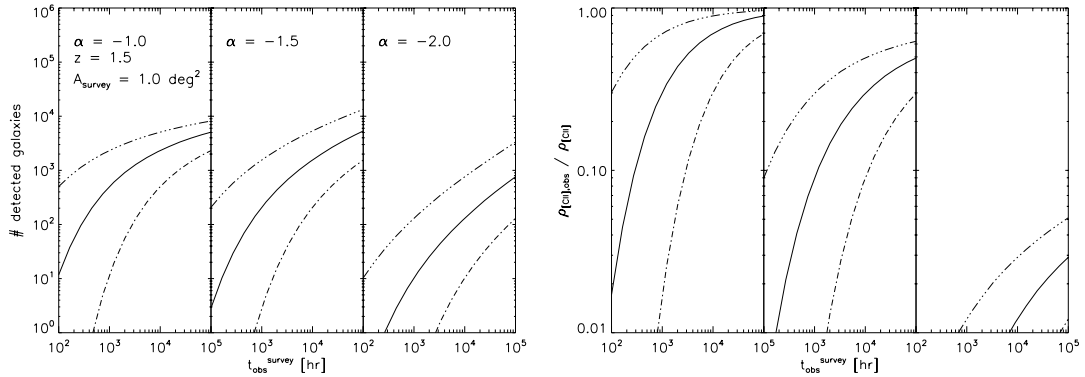


FIG. 8.—: The predicted number of [CII]-detected galaxies and observed fraction of [CII] intensity as a function of observing time for the square degree field. Solid, dash-triple-dotted, and dash-dotted curves represent the fiducial  $V_{pix}$ ,  $0.1V_{pix}$ , and  $10V_{pix}$ , resp.

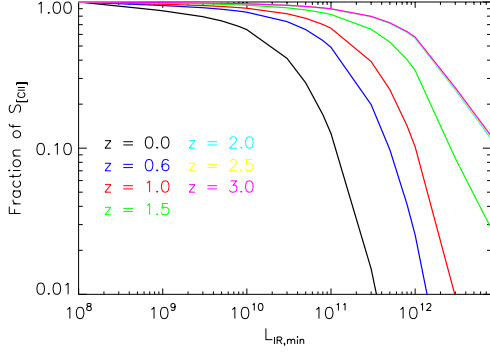


FIG. 9.—: The fraction of total [CII] mean intensity as a function of lower limit in the luminosity function. Different color curves represent different redshifts, as labeled on the plot.

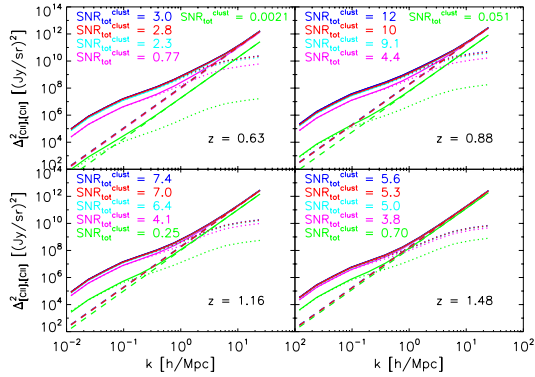


FIG. 10.—: Predicted [CII] power spectra from  $z = 0.63$  to  $z = 1.48$ . Blue, red, cyan, and magenta curves represent the power spectrum computed with a lower limit in the luminosity function corresponding to  $10^8$  (the fiducial lower limit),  $10^9$ ,  $10^{10}$ ,  $10^{11}$ , and  $10^{12}$   $L_{\odot}$ , respectively.